# Triplet superconductivity and spin density wave in biased AB bilayer graphene

A. O. Sboychakov, A. V. Rozhkov, and A. L. Rakhmanov
*Institute for Theoretical and Applied Electrodynamics, Russian Academy of Sciences, 125412 Moscow, Russia*

(Received 29 June 2023; revised 19 September 2023; accepted 27 September 2023; published 2 November 2023)

We examine spin density wave and triplet superconductivity as possible ground states of the Bernal bilayer graphene. The spin density wave is stable for the unbiased and undoped bilayer. Both the doping and the applied bias voltage destroy this phase. We show that, when biased and slightly doped, a bilayer can host a triplet superconducting phase. The mechanisms for both ordered phases rely on the renormalized Coulomb interaction. The consistency of our theoretical conclusions with recent experimental results is discussed.

DOI: 10.1103/PhysRevB.108.184503

## I. INTRODUCTION

The experimental observation of Mott insulating states and superconductivity in magic-angle twisted bilayer graphene [1–3] encouraged further studies of correlated phases in bilayer [4] and multilayer graphene systems. The most well-researched type of bilayer graphene is AB, or Bernal, bilayer graphene (AB-BLG). There is experimental evidence [5–8] that the ground state of AB-BLG is gapped even at zero bias voltage and zero doping, and the gap is of a many-body nature. The kind of ground state hosted by AB-BLG is under discussion. Different candidates for this low-temperature phase, such as ferromagnetic [9], spin-density wave (SDW) [10–12], "pseudomagnetic" [13], and nematic [14], among other possibilities, have been proposed.

Recently, a cascade of transitions between several nonsuperconducting states [15–17], as well as superconductivity [16], were observed in doped and biased AB-BLG. In Ref. [12], we argued theoretically that the transitions cascade reported in Refs. [15–17] can be connected to the sequence of several fractional metallic states (with spin and valley polarizations) that become stable in the doped SDW phase.

As for the AB-BLG superconducting phase, its transition temperature was experimentally estimated to be $T_c \approx 26$ mK. Curiously, the superconductivity appeared only when a magnetic field of about 150 mT was applied parallel to the bilayer. To explain the superconductivity in AB-BLG, both phonon [18,19] and electronic mechanisms [20–24] have been proposed.

Unlike our previous paper [12], which was dedicated to the nonsuperconducting states of the AB-BLG, here we focus on the superconductivity in the same system. Our starting point is the usual four-band tight-binding model with Coulomb interaction [4]. The model is studied using the zero-temperature mean-field approximation. To account for screening, the renormalized Coulomb potential is calculated within the random phase approximation (RPA). In contrast to similar approaches (see, e.g., Refs. [21,22]), we use the tight-binding model and distinguish intralayer and interlayer Coulomb potentials, which, as demonstrated below, experience dissimilar screening.

Our analysis begins with a mean-field study of the SDW phase in the undoped unbiased bilayer. Typically one expects that the SDW phase is more robust than superconductivity, which is indeed consistent with our findings. Thus, the SDW must be weakened to allow for stabilization of the superconductivity. Application of the bias voltage and doping favors the superconductivity. We prove that the renormalized Coulomb potential is enough to stabilize the triplet superconducting $p$-wave pairing in the AB-BLG. Our estimates for the superconducting state properties, and in particular $T_c$, are consistent with experiment.

The paper is organized as follows. In Sec. II the tight-binding Hamiltonian is described. Renormalized Coulomb interaction in unbiased undoped AB-BLG is calculated in Sec. III. We study the SDW phase in Sec. IV. Renormalized interaction for the doped biased bilayer is calculated in Sec. V. Section VI is dedicated to the superconducting phase. A more informal discussion of our findings, as well as the conclusions of our analysis, can be found in Sec. VII. Specific technical details are placed in two Appendixes.

## II. TIGHT-BINDING MODEL

In AB-BLG, carbon atoms in sublattice $B$ of the top layer are located right above the atoms of sublattice $A$ of the lower layer, while the atoms in sublattice $A$ of the top layer are located above the centers of the hexagons formed by the atoms of the lower layer. There are four atoms per unit cell. The elementary translation vectors for the AB-BLG can be chosen as $\mathbf{a}_{1,2} = a(\sqrt{3}, \mp 1)/2$, where $a = 2.46$ Å is the elementary unit length. Vector $\boldsymbol{\delta} = (\mathbf{a}_1 + \mathbf{a}_2)/3$ connects two atoms within a single unit cell in the same layer. The interlayer distance for AB-BLG is $d = 3.35$ Å.

We consider the following model Hamiltonian $H = H_0 + H_{\rm int}$, the first term being the single-particle Hamiltonian, while the second term describes the Coulomb interaction. These are

$$H_0 = \sum_{\mathbf{k}\sigma} \psi^\dagger_{\mathbf{k}\sigma} (\mathcal{H}_{\mathbf{k}} - \mu) \psi_{\mathbf{k}\sigma}, \tag{1}$$

$$H_{\rm int} = \frac{1}{2\mathcal{N}} \sum_{\substack{\mathbf{k}\mathbf{k}'\mathbf{q}\sigma\sigma' \\ ij\alpha\beta}} d^\dagger_{\mathbf{k}+\mathbf{q}i\alpha\sigma} d_{\mathbf{k}i\alpha\sigma} V^{ij}_{\mathbf{q}} d^\dagger_{\mathbf{k}'-\mathbf{q}j\beta\sigma'} d_{\mathbf{k}'j\beta\sigma'}. \tag{2}$$

 

In these equations, $\mu$ is the chemical potential, $\mathcal{N}$ is the number of unit cells in a bilayer sample, and the operators $d^\dagger_{\mathbf{k}i\alpha\sigma}$ and $d_{\mathbf{k}i\alpha\sigma}$ are the creation and annihilation operators of the electrons with momentum $\mathbf{k}$ in the layer $i$ $(=1,2)$, and in the sublattice $\alpha$ $(=A,B)$ with spin projection $\sigma$. The four-component operator-valued spinor $\psi^\dagger_{\mathbf{k}\sigma}$ is defined as

$$\psi^\dagger_{\mathbf{k}\sigma} = (d^\dagger_{\mathbf{k}1A\sigma},\, d^\dagger_{\mathbf{k}1B\sigma},\, d^\dagger_{\mathbf{k}2A\sigma},\, d^\dagger_{\mathbf{k}2B\sigma}), \tag{3}$$

and the $4\times 4$ matrix $\mathcal{H}_\mathbf{k}$ equals

$$\mathcal{H}_\mathbf{k} = \begin{pmatrix} e\Phi/2 & -tf_\mathbf{k} & 0 & t_0 \\ -tf^*_\mathbf{k} & e\Phi/2 & 0 & 0 \\ 0 & 0 & -e\Phi/2 & -tf_\mathbf{k} \\ t_0 & 0 & -tf^*_\mathbf{k} & -e\Phi/2 \end{pmatrix}, \tag{4}$$

where $e$ is the electron charge, $\Phi$ is the bias voltage, and the function $f_\mathbf{k}$ is

$$f_\mathbf{k} = e^{i\mathbf{k}\boldsymbol{\delta}}[1 + e^{-i\mathbf{k}\mathbf{a}_1} + e^{-i\mathbf{k}\mathbf{a}_2}]. \tag{5}$$

Parameter $t = 2.7$ eV is the in-plane nearest-neighbor hopping amplitude, and $t_0 = 0.4$ eV is the out-of-plane hopping amplitude between nearest-neighbor sites in positions $1A$ and $2B$. We choose the values of the hopping amplitudes $t$ and $t_0$ in accordance with Ref. [4].

It is important to note that in our model the interaction function $V^{ij}_\mathbf{q}$ in Eq. (2) is not a bare Coulomb electron-electron repulsion. It is a renormalized interaction, which accounts for many-body screening effects. It will be evaluated below using the RPA. As for electron-lattice coupling, it is ignored in our analysis.

We distinguish in the interaction Hamiltonian (2) the intralayer and interlayer couplings. This is done by introducing the layer indices in $V^{ij}_\mathbf{q}$. The interaction can be represented as a $2\times 2$ matrix. In such a matrix, the diagonal elements correspond to the intralayer interaction, while the off-diagonal elements correspond to the interlayer one.

Solving the eigenvalue/eigenvector problem $\mathcal{H}_\mathbf{k}\Psi_\mathbf{k} = \varepsilon_\mathbf{k}\Psi_\mathbf{k}$ for matrix (4), we obtain the single-particle spectrum of AB-BLG. It consists of the four bands

$$\begin{aligned}
\varepsilon^{(1)}_\mathbf{k} &= -\sqrt{t_\mathbf{k}^2 + \frac{e^2\Phi^2}{4} + \frac{t_0^2}{2} + \sqrt{t_\mathbf{k}^2\left(e^2\Phi^2 + t_0^2\right) + \frac{t_0^4}{4}}}, \\
\varepsilon^{(2)}_\mathbf{k} &= -\sqrt{t_\mathbf{k}^2 + \frac{e^2\Phi^2}{4} + \frac{t_0^2}{2} - \sqrt{t_\mathbf{k}^2\left(e^2\Phi^2 + t_0^2\right) + \frac{t_0^4}{4}}}, \\
\varepsilon^{(3)}_\mathbf{k} &= \sqrt{t_\mathbf{k}^2 + \frac{e^2\Phi^2}{4} + \frac{t_0^2}{2} - \sqrt{t_\mathbf{k}^2\left(e^2\Phi^2 + t_0^2\right) + \frac{t_0^4}{4}}}, \\
\varepsilon^{(4)}_\mathbf{k} &= \sqrt{t_\mathbf{k}^2 + \frac{e^2\Phi^2}{4} + \frac{t_0^2}{2} + \sqrt{t_\mathbf{k}^2\left(e^2\Phi^2 + t_0^2\right) + \frac{t_0^4}{4}}},
\end{aligned} \tag{6}$$

where $t_\mathbf{k} = t|f_\mathbf{k}|$. When $e\Phi = 0$, the spectrum near the Dirac points $\mathbf{K}_1 = (0, 4\pi/3a)$ and $\mathbf{K}_2 = -\mathbf{K}_1$ consists of four parabolic bands (two electron and two hole bands) with one electron and one hole band touching each other at Dirac points. At finite $e\Phi$ a single-particle gap opens, and the AB-BLG becomes an insulator.

The bispinor wave functions

$$\Psi^{(S)}_\mathbf{k} = \left(\Psi^{(S)}_{\mathbf{k}1A},\, \Psi^{(S)}_{\mathbf{k}1B},\, \Psi^{(S)}_{\mathbf{k}2A},\, \Psi^{(S)}_{\mathbf{k}2B}\right), \tag{7}$$

corresponding to the eigenvalues $\varepsilon^{(S)}_\mathbf{k}$, $S = 1,\ldots,4$, can be expressed analytically as well. However, the resultant formulas are quite cumbersome. In what follows, we will evaluate $\Psi^{(S)}_\mathbf{k}$ numerically.

It is useful to introduce new electronic operators $\gamma^\dagger_{\mathbf{k}S\sigma}$ and $\gamma_{\mathbf{k}S\sigma}$ according to

$$d_{\mathbf{k}i\alpha\sigma} = \sum_S \Psi^{(S)}_{\mathbf{k}i\alpha}\gamma_{\mathbf{k}S\sigma}. \tag{8}$$

Operator $\gamma^\dagger_{\mathbf{k}S\sigma}$ (operator $\gamma_{\mathbf{k}S\sigma}$) creates (destroys) an electron in an eigenstate with quasimomentum $\mathbf{k}$ in band $S$. In terms of these operators, the single-particle Hamiltonian reads

$$H_0 = \sum_{\mathbf{k}S\sigma}\left(\varepsilon^{(S)}_\mathbf{k} - \mu\right)\gamma^\dagger_{\mathbf{k}S\sigma}\gamma_{\mathbf{k}S\sigma}. \tag{9}$$

## III. POLARIZATION OPERATOR AND RENORMALIZED COULOMB POTENTIAL FOR UNDOPED BILAYER

Coulomb interaction in a solid experiences unavoidably strong renormalization due to screening. As already mentioned, we assume that the interaction function $V^{ij}_\mathbf{q}$ in Hamiltonian (2) incorporates static screening effects. To calculate $V^{ij}_\mathbf{q}$, the RPA can be used. It is commonly believed that for graphene-based systems, the RPA is a more appropriate approach due to the larger degeneracy factor $N_d = 4$.

A key element of any RPA scheme is a polarization operator. During two decades of theoretical research on graphene, numerous workers calculated the polarization operator for both biased and unbiased AB-BLG (see, e.g., Refs. [25–31]). In most of those publications, the effective two-band model of AB-BLG was employed. In Refs. [30,31], the polarization operator is calculated in the framework of a four-band model using the continuum approximation.

In this paper, we numerically evaluate the static polarization operator $\Pi^{ij}_\mathbf{q}$ for the four-band tight-binding model. Both intralayer $(i = j)$ and interlayer $(i \neq j)$ components will be determined. This is to be contrasted with the majority of the previous studies, which considered the total polarization operator $\Pi_\mathbf{q} = \sum_{ij}\Pi^{ij}_\mathbf{q}$ only.

The polarization operator of undoped AB-BLG can be presented as a $2\times 2$ matrix. The elements of this matrix as functions of the transferred momentum $\mathbf{q}$ read [31]

$$\begin{aligned}
\Pi^{ij}_\mathbf{q} = 2\sum_{SS'}\int\frac{d^2\mathbf{k}}{v_\mathrm{BZ}}&\frac{n_\mathrm{F}\left(\varepsilon^{(S)}_\mathbf{k}\right) - n_\mathrm{F}\left(\varepsilon^{(S')}_{\mathbf{k}+\mathbf{q}}\right)}{\varepsilon^{(S)}_\mathbf{k} - \varepsilon^{(S')}_{\mathbf{k}+\mathbf{q}}} \\
&\times\left(\sum_\alpha \Psi^{(S)}_{\mathbf{k}i\alpha}\Psi^{(S')*}_{\mathbf{k}+\mathbf{q}i\alpha}\right)\left(\sum_\beta \Psi^{(S)*}_{\mathbf{k}j\beta}\Psi^{(S')}_{\mathbf{k}+\mathbf{q}j\beta}\right),
\end{aligned} \tag{10}$$

where $S,\, S' = 1,\ldots,4$, $v_\mathrm{BZ} = 8\pi^2/(a^2\sqrt{3})$ is the Brillouin zone area, and $n_\mathrm{F}(E) = [e^{(E-\mu)/T} + 1]^{-1}$ is the Fermi function. We limit ourselves to zero temperature. The results of the numerical calculations of $\Pi^{ij}_\mathbf{q}$ are shown in Fig. 1 for two different values of $e\Phi$ ($e\Phi = 0$ and $e\Phi = 0.01t_0$).

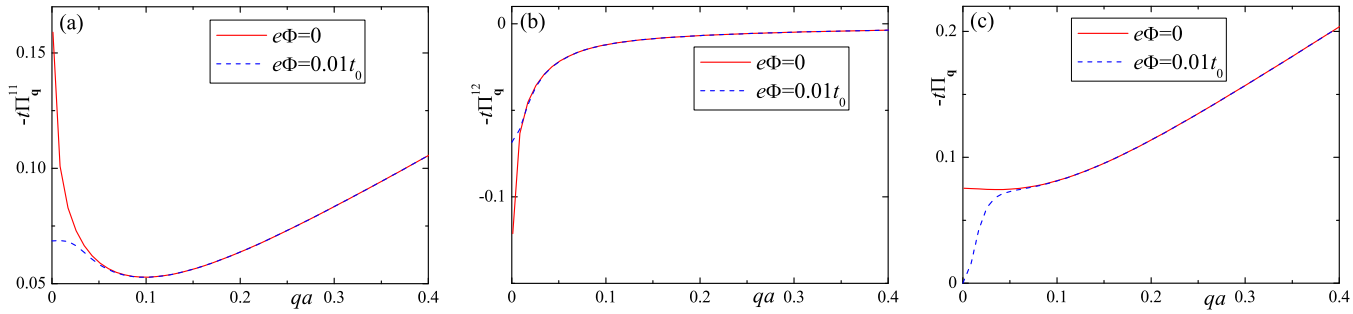


FIG. 1. The polarization operator components of undoped AB-BLG as functions of the momentum $\mathbf{q}$ for $\mathbf{q} = q(1,\ 0)$. Panels (a), (b), and (c) show $\Pi^{11}_{\mathbf{q}}$, $\Pi^{12}_{\mathbf{q}}$, and the total polarization operator $\Pi_{\mathbf{q}} = \sum_{ij} \Pi^{ij}_{\mathbf{q}}$, respectively. The curves in all panels are calculated for $\mu = 0$. Solid (red) curves correspond to $e\Phi = 0$, while dashed (blue) curves correspond to $e\Phi = 0.01t_0$.

Analyzing the numerical data, we observe that $\Pi^{11}_{\mathbf{q}} = \Pi^{22}_{\mathbf{q}}$, which a manifestation of the charge-conjugation symmetry (see also Appendix A). Furthermore, as long as $q = |\mathbf{q}|$ is not too large, $qa < 1$, the polarization operator is virtually independent of the direction of $\mathbf{q}$. From Fig. 1 we see that the intralayer components $\Pi^{11}_{\mathbf{q}}$ and $\Pi^{22}_{\mathbf{q}}$ are always negative, while $\Pi^{12}_{\mathbf{q}}$ is positive. For small $q$, the value of $-\Pi^{11}_{\mathbf{q}}$ decreases with the increase of $q$. This decay is replaced by a linear growth at larger $q$, which is similar to the behavior of the polarization operator of single-layer graphene [32]. The interlayer polarization $\Pi^{12}_{\mathbf{q}}$ monotonously decreases with $q$. Asymptotically, it behaves as $1/q$ at $qa > 0.1$.

The renormalized Coulomb interaction can be expressed in matrix form as

$$\hat{V}_{\mathbf{q}} = \hat{V}^{(0)}_{\mathbf{q}}\big(1 - \hat{\Pi}_{\mathbf{q}}\hat{V}^{(0)}_{\mathbf{q}}\big)^{-1}. \tag{11}$$

In this formula, the bare Coulomb interaction is a $2 \times 2$ matrix

$$\hat{V}^{(0)}_{\mathbf{q}} = \frac{A}{q}\begin{pmatrix} 1 & e^{-qd} \\ e^{-qd} & 1 \end{pmatrix}, \quad A = \frac{2\pi e^2}{\mathcal{S}_{\rm gr}\epsilon}, \tag{12}$$

where $\mathcal{S}_{\rm gr} = a^2\sqrt{3}/2$ is the area of the graphene unit cell, and $\epsilon$ is the dielectric constant of the media surrounding the graphene sample. Thus, we obtain

$$V^{11}_{\mathbf{q}} = V^{22}_{\mathbf{q}} = A\frac{1 - \frac{A}{q}\Pi^{22}_{\mathbf{q}}[1 - e^{-2qd}]}{q - A\big(\Pi^{11}_{\mathbf{q}} + \Pi^{22}_{\mathbf{q}} + 2e^{-qd}\Pi^{12}_{\mathbf{q}}\big) + \frac{A^2}{q}\big[\Pi^{11}_{\mathbf{q}}\Pi^{22}_{\mathbf{q}} - \big(\Pi^{12}_{\mathbf{q}}\big)^2\big][1 - e^{-2qd}]}, \tag{13}$$

$$V^{12}_{\mathbf{q}} = V^{21}_{\mathbf{q}} = A\frac{e^{-qd} + \frac{A}{q}\Pi^{12}_{\mathbf{q}}[1 - e^{-2qd}]}{q - A\big(\Pi^{11}_{\mathbf{q}} + \Pi^{22}_{\mathbf{q}} + 2e^{-qd}\Pi^{12}_{\mathbf{q}}\big) + \frac{A^2}{q}\big[\Pi^{11}_{\mathbf{q}}\Pi^{22}_{\mathbf{q}} - \big(\Pi^{12}_{\mathbf{q}}\big)^2\big][1 - e^{-2qd}]}. \tag{14}$$

Similar results can be found in the literature on the Coulomb drag in two-dimensional systems; see, for example, Refs. [33,34].

At zero bias we have $\Pi^{11}_{\mathbf{q}} + \Pi^{12}_{\mathbf{q}} \neq 0$ at $q \to 0$ (which is consistent with the results obtained in Ref. [28]). Thus, the matrix $\hat{V}_{\mathbf{q}}$ is regular at $q \to 0$. In other words, the screened Coulomb potential is finite at $q = 0$, which agrees with a general expectation that the finite density of states at the Fermi energy leads to the suppression of the long-range Coulomb interaction.

When $e\Phi \neq 0$, the single-electron spectrum acquires a gap that affects the low-$q$ screening. Indeed, in this regime, $(\Pi^{11}_{\mathbf{q}} + \Pi^{12}_{\mathbf{q}})|_{\mathbf{q}=0} = 0$, thus the matrix $\hat{V}_{\mathbf{q}}$ is singular at $q = 0$. This singularity indicates that in the insulating state of the biased AB-BLG, the long-range interaction cannot be completely screened and the resultant Coulomb potential behaves as $V^{ij}_{\mathbf{q}} \propto 1/q$ at small $q$. However, such a behavior persists for small momenta only. Additional details can be learned from Fig. 2 where numerically calculated $V^{ij}_{\mathbf{q}}$ is plotted for $e\Phi = 0$ and $e\Phi = 0.01t_0$.

Concluding this section, we would like to make the following observation. If $d \to 0$, then Eqs. (13) and (14) are replaced by one simple formula,

$$V^{ij}_{\mathbf{q}} = \frac{A}{q - A\Pi_{\mathbf{q}}}. \tag{15}$$

The right-hand side of this expression is independent of $i$ and $j$. In other words, such an approximation implies that the interlayer and intralayer interactions are identical. In the literature, theoretical results essentially similar to Eq. (15) are not uncommon (see, for example, Refs. [25,26,28], to name a few). Unfortunately, the reliability of this approximation is not clear: our numerical data suggest that formula (15) is a rather crude simplification that is poorly applicable even in the limit of small $q$. More details can be found in Appendix B.

## IV. SPIN-DENSITY-WAVE STATE

The computed renormalized Coulomb interaction can be applied to the study of the AB-BLG ordered states. We characterize the SDW by the following expectation value:

$$\eta^{\rm SDW}_{\mathbf{k}} = \langle \gamma^{\dagger}_{\mathbf{k}3\bar{\sigma}}\gamma_{\mathbf{k}2\sigma}\rangle, \tag{16}$$

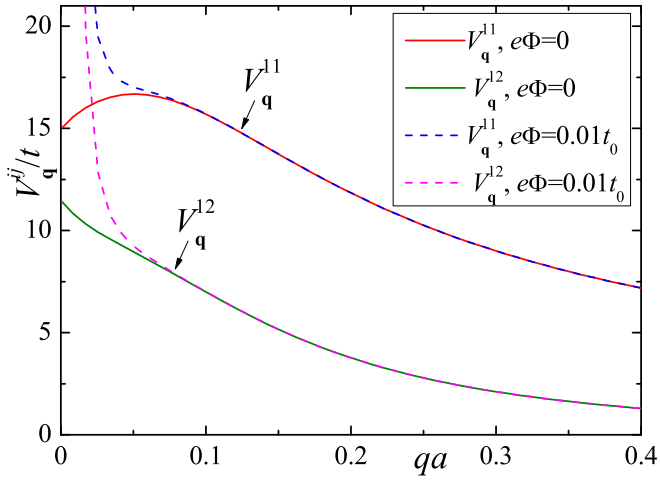


FIG. 2. The renormalized interaction components as functions of the momentum $q$, at $\mathbf{q} = q(1, 0)$, calculated for undoped AB-BLG ($\mu = 0$) and two values of the bias potential $e\Phi$. Diagonal components $V^{11}_{\mathbf{q}} = V^{22}_{\mathbf{q}}$ are plotted as red and blue curves; off diagonal $V^{12}_{\mathbf{q}} = V^{21}_{\mathbf{q}}$ components are plotted as green and magenta curves. The solid (dashed) curves represent the $e\Phi = 0$ case ($e\Phi = 0.01t_0$ case). For all curves, $\epsilon = 1$.

which we assumed to be independent of $\sigma$ (the bar over $\sigma$ means not $\sigma$). This relation implies that in our SDW state, a hole in the band $S = 2$ is coupled to an electron with opposite spin in the band $S = 3$.

Equation (8) allows us to express $H_{\rm int}$ in terms of the band operators $\gamma^\dagger_{\mathbf{k}S\sigma}$, $\gamma_{\mathbf{k}S\sigma}$. Keeping only the terms relevant to the SDW pairing, one derives

$$H_{\rm int} = -\frac{1}{2\mathcal{N}}\sum_{\mathbf{k}\mathbf{k}'\sigma}\big(\gamma^\dagger_{\mathbf{k}2\sigma}\gamma_{\mathbf{k}3\bar\sigma}\Gamma^{(1)}_{\mathbf{k}\mathbf{k}'}\gamma^\dagger_{\mathbf{k}'3\bar\sigma}\gamma_{\mathbf{k}'2\sigma} + \gamma^\dagger_{\mathbf{k}2\sigma}\gamma_{\mathbf{k}3\bar\sigma}\Gamma^{(2)}_{\mathbf{k}\mathbf{k}'}\gamma^\dagger_{\mathbf{k}'2\bar\sigma}\gamma_{\mathbf{k}'3\sigma} + \text{H.c.}\big), \tag{17}$$

where

$$\Gamma^{(1)}_{\mathbf{k}\mathbf{k}'} = \sum_{ij}\left(\sum_\alpha \Psi^{(2)*}_{\mathbf{k}i\alpha}\Psi^{(2)}_{\mathbf{k}'i\alpha}\right)V^{ij}_{\mathbf{k}-\mathbf{k}'}\left(\sum_\beta \Psi^{(3)}_{\mathbf{k}j\beta}\Psi^{(3)*}_{\mathbf{k}'j\beta}\right),$$
$$\Gamma^{(2)}_{\mathbf{k}\mathbf{k}'} = \sum_{ij}\left(\sum_\alpha \Psi^{(2)*}_{\mathbf{k}i\alpha}\Psi^{(3)}_{\mathbf{k}'i\alpha}\right)V^{ij}_{\mathbf{k}-\mathbf{k}'}\left(\sum_\beta \Psi^{(3)}_{\mathbf{k}j\beta}\Psi^{(2)*}_{\mathbf{k}'j\beta}\right). \tag{18}$$

Note that Eq. (17) ignores retardation effects in screening physics, implying that the screening is instantaneous. The validity of this approximation will be discussed in Sec. VII B.

Introducing the SDW order parameter as

$$\Delta^{\rm SDW}_{\mathbf{k}} = \frac{1}{\mathcal{N}}\sum_{\mathbf{k}'}\big(\Gamma^{(1)}_{\mathbf{k}\mathbf{k}'}\eta^{\rm SDW}_{\mathbf{k}'} + \Gamma^{(2)}_{\mathbf{k}\mathbf{k}'}\eta^{\rm SDW*}_{\mathbf{k}'}\big), \tag{19}$$

and performing the standard mean-field decoupling scheme in Eq. (17), we obtain the mean-field Hamiltonian, which allows us to calculate the grand potential $\Omega$. Minimization of $\Omega$ gives the following equation for the SDW order parameter:

$$\Delta^{\rm SDW}_{\mathbf{k}} = \int\frac{d^2\mathbf{k}'}{v_{\rm BZ}}\frac{\Gamma^{(1)}_{\mathbf{k}\mathbf{k}'}\Delta^{\rm SDW}_{\mathbf{k}'} + \Gamma^{(2)}_{\mathbf{k}\mathbf{k}'}\Delta^{\rm SDW*}_{\mathbf{k}'}}{2\sqrt{\big[\varepsilon^{(3)}_{\mathbf{k}'}\big]^2 + \big|\Delta^{\rm SDW}_{\mathbf{k}'}\big|^2}}. \tag{20}$$

Let us consider first the case of $e\Phi = 0$. We do not solve the integral equation (20) directly. Instead, we perform a transparent and physically motivated approximate evaluation of $\Delta^{\rm SDW}_{\mathbf{k}}$. First, we observe that the main contribution to the integral on the right-hand side of Eq. (20) comes from momenta $\mathbf{k}'$ near the Dirac points $\mathbf{K}_\xi$ ($\xi = 1, 2$). Thus, it is necessary to know the behavior of $\Gamma^{(1)}_{\mathbf{k}\mathbf{k}'}$ and $\Gamma^{(2)}_{\mathbf{k}\mathbf{k}'}$ with momenta $\mathbf{k}$ and $\mathbf{k}'$ close to $\mathbf{K}_\xi$. It is possible to show that, for $e\Phi = 0$, the wave functions $\Psi^{(2,3)}_{\mathbf{k}\alpha}$ near the Dirac point $\mathbf{K}_\xi$ are

$$\Psi^{(2)}_{\mathbf{K}_\xi+\mathbf{p}i\alpha} = \frac{1}{\sqrt{2}}\begin{pmatrix}0\\ e^{-i[\frac{\pi}{2}-(-1)^\xi\phi_{\mathbf{p}}]}\\ e^{i[\frac{\pi}{2}-(-1)^\xi\phi_{\mathbf{p}}]}\\ 0\end{pmatrix},$$
$$\Psi^{(3)}_{\mathbf{K}_\xi+\mathbf{p}i\alpha} = \frac{1}{\sqrt{2}}\begin{pmatrix}0\\ -e^{-i[\frac{\pi}{2}-(-1)^\xi\phi_{\mathbf{p}}]}\\ e^{i[\frac{\pi}{2}-(-1)^\xi\phi_{\mathbf{p}}]}\\ 0\end{pmatrix}, \tag{21}$$

where $\phi_{\mathbf{p}}$ is the polar angle of the vector $\mathbf{p} \to \mathbf{0}$. Substituting these equations in formulas (18), we approximate $\Gamma^{(1,2)}_{\mathbf{K}_\xi+\mathbf{p}\mathbf{K}_\xi+\mathbf{p}'}$ for small $|\mathbf{p}|$ and $|\mathbf{p}'|$ as

$$\tilde\Gamma^{(1,2)}_{\mathbf{p}\mathbf{p}'} \approx \tfrac{1}{2}\big\{V^{11}_{\mathbf{p}-\mathbf{p}'} \pm V^{12}_{\mathbf{p}-\mathbf{p}'}\cos[2(\phi_{\mathbf{p}} - \phi_{\mathbf{p}'})]\big\}. \tag{22}$$

Here and below, the tilde over a function of momentum indicates that the momentum is measured from the Dirac point $\mathbf{K}_\xi$. The approximate quantities $\tilde\Gamma^{(1,2)}_{\mathbf{p}\mathbf{p}'}$ are the same in both valleys, consequently the dependence on $\xi$ is suppressed. Additionally, Eq. (22) implies that $\tilde\Gamma^{(1,2)}_{\mathbf{p}\mathbf{p}'}$ are real functions of momenta $\mathbf{p}$ and $\mathbf{p}'$ when $\mathbf{p}$, $\mathbf{p}'$ are close to a Dirac point. Therefore, one can expect that the SDW order parameter is also a real function of $\mathbf{p}$.

To estimate the SDW order parameter, we assume that $\Delta^{\rm SDW}_{\mathbf{k}}$ is a step function of the momentum inside some region near each Dirac point, that is,

$$\Delta^{\rm SDW}_{\mathbf{K}_\xi+\mathbf{p}} = \begin{cases}\Delta^{\rm SDW}, & |\mathbf{p}| < K_0,\\ 0, & |\mathbf{p}| > K_0,\end{cases} \tag{23}$$

where the cutoff momentum $K_0$ is chosen such that the regions corresponding to different Dirac points do not intersect. Below we neglect coupling of the order parameters from different valleys and assume that $\mathbf{k}$ and $\mathbf{k}'$ in Eq. (20) lie in the same valley. Taking $\mathbf{k} = \mathbf{K}_\xi$ and using the ansatz (23), one derives the equation for $\Delta^{\rm SDW}$,

$$\int_{|\mathbf{p}|<K_0}\frac{d^2\mathbf{p}}{v_{\rm BZ}}\frac{\tilde\Gamma^{(1)}_{0\mathbf{p}} + \tilde\Gamma^{(2)}_{0\mathbf{p}}}{2\sqrt{\big[\tilde\varepsilon^{(3)}_{\mathbf{p}}\big]^2 + (\Delta^{\rm SDW})^2}} = 1. \tag{24}$$

We solve this equation numerically, taking $K_0$ by its maximum possible value $K_0 = 2\pi/(3a)$. We choose $\epsilon = 1$. Other parameters are fixed as explained above. In so doing, we obtain $\Delta^{\rm SDW} = 0.0018t = 4.9$ meV. This result is in agreement with experimentally available data, Ref. [7], where the measured transport gap in the Bernal bilayer graphene, which is twice the order parameter, is equal to $\Delta_{\rm tr} = 8$ meV.

In our approach, the SDW order arises due to the long-range Coulomb interaction. Thus, the result is sensitive to the value of the dielectric constant: if $\epsilon$ is increased, the order parameter decreases. For example, for $\epsilon = 5$, we find that

$\Delta^{\mathrm{SDW}} = 0.15$ meV, which is about 30 times smaller than the value of $\Delta^{\mathrm{SDW}}$ at $\epsilon = 1$.

Consider now the case of $e\Phi \neq 0$. At finite bias, the gap between bands 2 and 3 arises even in the single-particle approximation. Therefore, one can expect that the bias voltage destroys the SDW ordering. Indeed, if the gap is open, the denominator in Eq. (20) never reaches zero even in the limit of $\Delta^{\mathrm{SDW}} \to 0$. As a result, we obtain from $\Delta^{\mathrm{SDW}} \to 0$ the following criterion for the existence of the SDW ordering at finite bias voltage:

$$\int_{|\mathbf{p}|<K_0} \frac{d^2\mathbf{p}}{v_{\mathrm{BZ}}} \frac{\tilde{\Gamma}^{(1)}_{\mathbf{p}'\mathbf{p}} + \tilde{\Gamma}^{(2)}_{\mathbf{p}'\mathbf{p}}}{2\tilde{\varepsilon}^{(3)}_{\mathbf{p}}} > 1, \tag{25}$$

where the momentum $\mathbf{p}'$ is to be chosen to maximize the integral. The values $V^{ij}_{\mathbf{q}}$ for $e\Phi = 0$ and $e\Phi \neq 0$ almost coincide at larger $q$ (see Fig. 2) and we assume that $e\Phi$ is small enough. Then, in Eq. (25) we can use the functions $\Gamma^{(1,2)}_{\mathbf{k}\mathbf{k}'}$ calculated at $e\Phi = 0$ (divergence of $V^{ij}_{\mathbf{q}}$ for $e\Phi \neq 0$ at $q \to 0$ is an integrable one). In this case, one can take $\mathbf{k} = \mathbf{K}_\xi$, or, equivalently, $\mathbf{p}' = 0$ in Eq. (25).

Numerical analysis shows that SDW ordering is completely suppressed for $e\Phi > e\Phi_c$, where the critical bias value is found to be $e\Phi_c = 0.0038t = 0.025t_0 = 10$ meV at $\epsilon = 1$. Thus, we obtain the quite natural result that the critical bias voltage $e\Phi_c$ is of the order of $\Delta^{\mathrm{SDW}}$ calculated at $e\Phi = 0$.

## V. POLARIZATION OPERATOR AND RENORMALIZED COULOMB POTENTIAL FOR DOPED BILAYER

The nonsuperconducting ordered state (for example, the SDW discussed above, or a similar phase) is expected to dominate any superconducting state in pristine graphene-based systems. Indeed, experimentally measured energy scales associated with nonsuperconducting ordered phases are in the range of several meV (see, for example, Refs. [6,7,35,36]), while the relevant superconducting energy is several orders of magnitude lower [16]. Consequently, it is necessary to suppress a nonsuperconducting order parameter to make superconductivity possible.

The suppression of the SDW by the bias voltage, considered in Sec. IV, is not suitable since it leads to a change from the SDW insulator to the band insulator. A more convenient approach is doping. Doping destroys the SDW ordering, replacing it by a metal with a well-developed Fermi surface.

The presence of a Fermi surface drastically changes the screening properties of AB-BLG. To account for these, we present here the results of our numerical calculations of the polarization operator and renormalized Coulomb potential of the doped and biased bilayer graphene. We consider an electron doping and assume that under doping only the band $S = 3$ crosses the Fermi level $\mu$, while the band $S = 4$ remains empty. It is also assumed that the following restriction on the chemical potential is met: $\mu_{\min} < \mu < \mu_{\max}$, where $\mu_{\min} = e\Phi t_0/(2\sqrt{e^2\Phi^2 + t_0^2})$ and $\mu_{\max} = e\Phi/2$. In this case, the Fermi surface consists of four approximately circular pockets. A pair of these, with Fermi momenta $k_{\mathrm{F}}^{(1)}$ and $k_{\mathrm{F}}^{(2)}$, are centered at Dirac point $\mathbf{K}_1$. An identical pair is centered at $\mathbf{K}_2$. Using Eq. (6) and linear expansion $|t_{\mathbf{k}}| \approx v_F k$, where $v_F = \sqrt{3}ta/2$ is the graphene Fermi velocity, we derive an

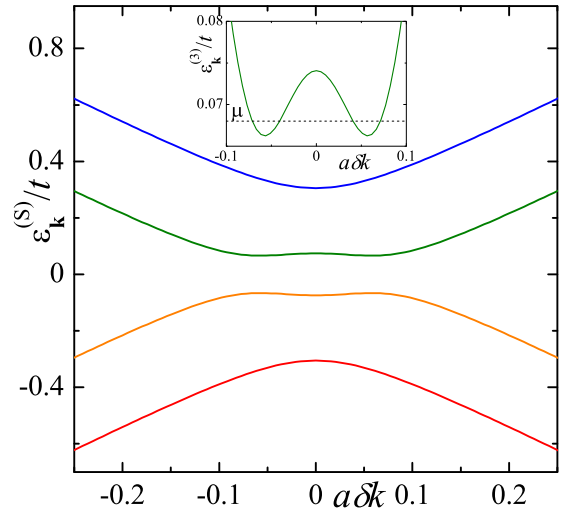


FIG. 3. Band structure of the biased bilayer graphene near the Dirac point, calculated at $e\Phi = 0.5t_0$. Four bands $S = 1, \ldots, 4$ are plotted as functions of the deviation of momentum from the Dirac point $\delta k$. The inset shows the fine structure of the band $\varepsilon^{(3)}_{\mathbf{k}}$ close to the Dirac point. The horizontal dashed line is the position of the chemical potential $\mu$.

expression for the Fermi momenta $k_{\mathrm{F}}^{(1)}$ and $k_{\mathrm{F}}^{(2)}$,

$$k_{\mathrm{F}}^{(1,2)} = \frac{1}{v_{\mathrm{F}}} \sqrt{\frac{e^2\Phi^2}{4} + \mu^2 \mp \sqrt{e^2\Phi^2\mu^2 + \left(\mu^2 - \frac{e^2\Phi^2}{4}\right)t_0^2}}. \tag{26}$$

Each inner Fermi surface is holelike, while the outer one is electronlike. Absolute values of the Fermi velocities at each Fermi surface are equal to ($s = 1, 2$)

$$v_{\mathrm{F}}^{(s)} = \frac{v_{\mathrm{F}}^2 k_{\mathrm{F}}^{(s)}}{\mu} \left| 1 - \frac{e^2\Phi^2 + t_0^2}{\sqrt{4\left[v_{\mathrm{F}}k_{\mathrm{F}}^{(s)}\right]^2\left(e^2\Phi^2 + t_0^2\right) + t_0^4}} \right|. \tag{27}$$

When $\mu \to \mu_{\min}$, these velocities vanish, $v_{\mathrm{F}}^{(s)} \to 0$, and the density of states at the Fermi level diverges. The band structure near the Dirac point $\mathbf{K}_1$ and the typical position of the chemical potential are plotted in Fig. 3.

The electron concentration (per one site) is a function of $\mu$ and can be expressed as

$$x = \frac{1}{2}\int \frac{d^2\mathbf{k}}{v_{\mathrm{BZ}}} \Theta\left(\mu - \varepsilon^{(3)}_{\mathbf{k}}\right) \approx \frac{\pi}{v_{\mathrm{BZ}}}\left[\left(k_{\mathrm{F}}^{(2)}\right)^2 - \left(k_{\mathrm{F}}^{(1)}\right)^2\right], \tag{28}$$

where $\Theta(E)$ is the Heaviside step function.

The numerical analysis of Eq. (10) shows that the doping substantially modifies the polarization operator at small $q$ and the change comes mainly from the intraband term (the term with $S = S' = 3$) in Eq. (10), which is zero if $\mu = 0$. The bias voltage breaks the symmetry between graphene layers. As a result, extra charge introduced by the doping accumulates mainly, say, in layer 1. Thus, we have $\Pi^{11}_{\mathbf{q}} \neq \Pi^{22}_{\mathbf{q}}$. It turns out that $|\Pi^{11}_{\mathbf{q}}| \gg |\Pi^{22}_{\mathbf{q}}| \sim |\Pi^{12}_{\mathbf{q}}|$ at small $q$, that is, the screening in layer 1 is much greater than that in layer 2. The dependencies of $\Pi^{11}_{\mathbf{q}}$, $\Pi^{22}_{\mathbf{q}}$, and $\Pi^{12}_{\mathbf{q}}$ on $q$ are shown in Fig. 4. We clearly see three Kohn anomalies located at momenta $q = k_{\mathrm{F}}^{(2)} - k_{\mathrm{F}}^{(1)}$,

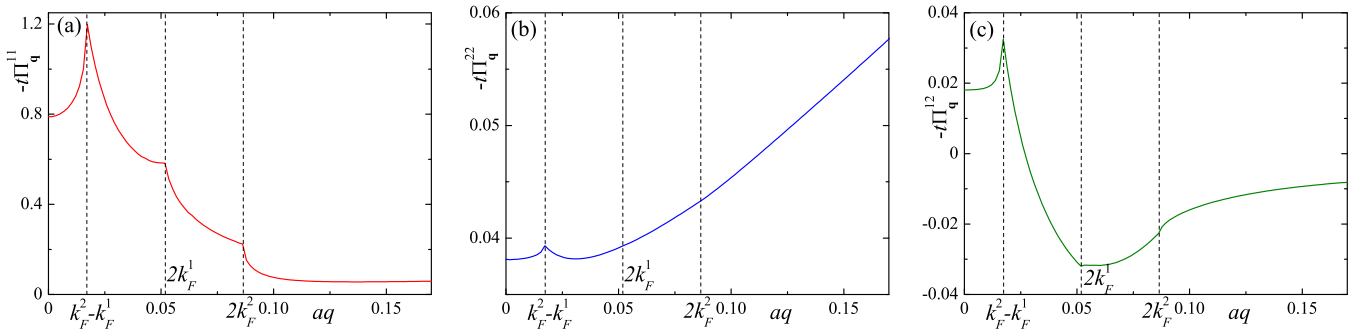


FIG. 4. The polarization operator components for biased doped AB-BLG, as functions of the momentum $\mathbf{q}$, for $\mathbf{q} = q(1, 0)$. Panels (a), (b), and (c) show $\Pi_{\mathbf{q}}^{11}$, $\Pi_{\mathbf{q}}^{22}$, and $\Pi_{\mathbf{q}}^{12}$, respectively. The curves in all panels are calculated for $e\Phi = 0.3t_0$ and $\mu = 0.021t$.

$q = 2k_{\mathrm{F}}^{(1)}$, and $q = 2k_{\mathrm{F}}^{(2)}$. Under doping, the value of $\Pi_{\mathbf{q}}^{12}$ is negative at small $q$ for a definite doping level; in this case, it changes sign at some value of $q$. The polarization component $\Pi_{\mathbf{q}}^{11}$ is the main contributor to the total polarization $\Pi_{\mathbf{q}}$. The dependence of $\Pi_{\mathbf{q}}$ on $q$ computed in this work is consistent with the results obtained in the framework of the four-band continuum model in Ref. [31].

The typical dependence of $V_{\mathbf{q}}^{ij}$ on $q$ (for $\epsilon = 1$) at finite doping and bias voltage is shown in Fig. 5. In this regime, $\Pi_{\mathbf{q}}^{11} \neq \Pi_{\mathbf{q}}^{22}$, consequently $V_{\mathbf{q}}^{11} \neq V_{\mathbf{q}}^{22}$. When $q \lesssim 2k_{\mathrm{F}}^{(2)}$, we have $V_{\mathbf{q}}^{11} \ll V_{\mathbf{q}}^{22}$. At small $q$ the screening in layer 2 is the weakest, thus the interaction inside this layer is the strongest. The screening effects of the carriers introduced by doping become less important for larger $q$, where $V_{\mathbf{q}}^{11}$ and $V_{\mathbf{q}}^{22}$ are of the same order.

The important feature of the curves shown in Fig. 5 is that, when $q \lesssim 2k_{\mathrm{F}}^{(2)}$, the interaction $V_{\mathbf{q}}^{ij}$ increases with $q$. As we will prove in the next section, such a behavior is sufficient to stabilize a triplet superconducting state.

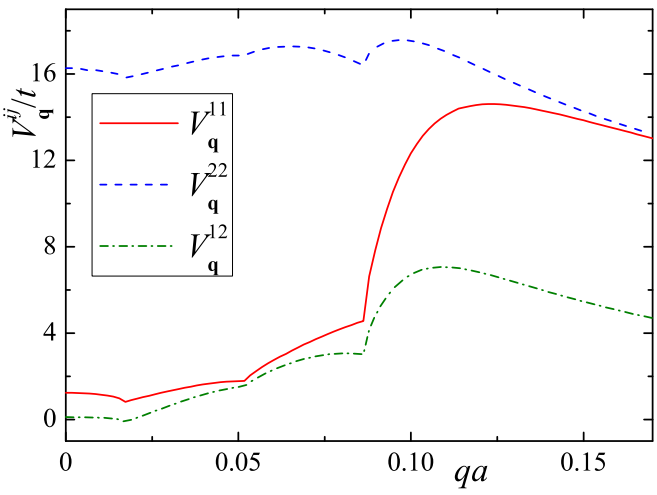


FIG. 5. The renormalized interaction components at finite doping as functions of the momentum $\mathbf{q}$ for $\mathbf{q} = q(1, 0)$. The curves are calculated at $e\Phi = 0.3t_0$ and $\mu = 0.0021t$. Components $V_{\mathbf{q}}^{11}$, $V_{\mathbf{q}}^{22}$, and $V_{\mathbf{q}}^{12}$ are plotted as a (red) solid curve, a (blue) dashed curve, and a (green) dash-dotted curve, respectively. All curves are computed at $\epsilon = 1$.

## VI. TRIPLET SUPERCONDUCTIVITY

The following consideration of superconductivity in biased, and doped bilayer graphene assumes that the bias voltage $e\Phi$ exceeds the critical value $e\Phi_c$, thus the SDW state is suppressed. The type of superconductivity considered herein arises due to Coulomb interaction. In contrast to the usual BCS $s$-wave superconductivity, this phase exists only in the $p$-wave channel, as will be discussed below.

To derive the mean-field form of the model, we rewrite the interaction Hamiltonian (2) in the form

$$H_{\mathrm{int}} = \frac{1}{2\mathcal{N}} \sum_{\substack{\mathbf{k}\mathbf{k}'\sigma\sigma' \\ ij\alpha\beta}} d_{\mathbf{k}i\alpha\sigma}^{\dagger} d_{-\mathbf{k}j\beta\sigma}^{\dagger} V_{\mathbf{k}-\mathbf{k}'}^{ij} d_{-\mathbf{k}'j\beta\sigma'} d_{\mathbf{k}'i\alpha\sigma'}, \tag{29}$$

where all contributions unimportant for the superconductivity are omitted. Substituting Eq. (8) in the formula above and keeping only terms with $S = 3$, one obtains

$$H_{\mathrm{int}} = \frac{1}{2\mathcal{N}} \sum_{\substack{\mathbf{k}\mathbf{k}'\sigma\sigma' \\ ij\alpha\beta}} \gamma_{\mathbf{k}3\sigma}^{\dagger} \gamma_{-\mathbf{k}3\sigma}^{\dagger} \Gamma_{\mathbf{k}\mathbf{k}'}^{\mathrm{SC}} \gamma_{-\mathbf{k}'3\sigma'} \gamma_{\mathbf{k}'3\sigma}, \tag{30}$$

where

$$\Gamma_{\mathbf{k}\mathbf{k}'}^{\mathrm{SC}} = \sum_{ij} \left( \sum_{\alpha} \Psi_{\mathbf{k}i\alpha}^{(3)*} \Psi_{\mathbf{k}'i\alpha}^{(3)} \right) V_{\mathbf{k}-\mathbf{k}'}^{ij} \left( \sum_{\beta} \Psi_{-\mathbf{k}j\beta}^{(3)*} \Psi_{-\mathbf{k}'j\beta}^{(3)} \right). \tag{31}$$

The role of $\Gamma_{\mathbf{k}\mathbf{k}'}^{\mathrm{SC}}$ in the theory of the superconducting phase is analogous to the role of $\Gamma_{\mathbf{k}\mathbf{k}'}^{(1,2)}$ for the SDW; see Sec. IV.

Similar to Eq. (17), we ignored screening retardation in Eq. (30) as well. For more discussion, see Sec. VII B.

We assume that our triplet ($p$-wave) superconducting state is characterized by the following anomalous expectation values:

$$\eta_{\mathbf{k}}^{\mathrm{SC}} = \langle \gamma_{-\mathbf{k}3\uparrow} \gamma_{\mathbf{k}3\uparrow} \rangle = \langle \gamma_{-\mathbf{k}3\downarrow} \gamma_{\mathbf{k}3\downarrow} \rangle. \tag{32}$$

This specific choice is one possibility among many; others are connected to Eq. (32) through unitary transformations representing O(3) rotations of electron spin. The superconducting order parameter can be defined as

$$\Delta_{\mathbf{k}}^{\mathrm{SC}} = \frac{1}{\mathcal{N}} \sum_{\mathbf{k}'} \Gamma_{\mathbf{k}\mathbf{k}'}^{\mathrm{SC}} \eta_{\mathbf{k}'}^{\mathrm{SC}}. \tag{33}$$

When momentum $\mathbf{k}$ is close to the Dirac point $\mathbf{K}_\xi$, the expectation value $\eta^{\rm SC}_{\mathbf{k}}$ couples electrons belonging to different valleys. Since $\eta^{\rm SC}_{\mathbf{k}}$ couples electrons with the same spin, one has

$$\eta^{\rm SC}_{-\mathbf{k}} = -\eta^{\rm SC}_{\mathbf{k}} \quad \Leftrightarrow \quad \Delta^{\rm SC}_{-\mathbf{k}} = -\Delta^{\rm SC}_{\mathbf{k}}. \tag{34}$$

Indeed, as the spin part of the Cooper pair wave function is even, the orbital wave function must be odd.

Performing the standard mean-field decoupling in Eq. (30) and minimizing the grand potential, we derive the zero-temperature self-consistency equation for $\Delta^{\rm SC}_{\mathbf{k}}$,

$$\Delta^{\rm SC}_{\mathbf{k}} = -\int \frac{d^2\mathbf{k}'}{v_{\rm BZ}} \frac{\Gamma^{\rm SC}_{\mathbf{k}\mathbf{k}'}\Delta^{\rm SC}_{\mathbf{k}'}}{2\sqrt{\left[\varepsilon^{(3)}_{\mathbf{k}'} - \mu\right]^2 + \left|\Delta^{\rm SC}_{\mathbf{k}'}\right|^2}}. \tag{35}$$

The minus sign on the right-hand side of the self-consistency equation is due to the repulsive Coulomb interaction. However, as we will show below, the right-hand side of Eq. (35) can be positive for the specific choice of the form of the order parameter.

The main contribution to the integral in Eq. (35) comes from the momenta $\mathbf{k}'$ near each Dirac point. In these regions, it is convenient to define

$$\tilde{\varepsilon}_p = \varepsilon^{(3)}_{\mathbf{K}_\xi + \mathbf{p}}, \tag{36}$$

where

$$\tilde{\varepsilon}_p = \sqrt{v_{\rm F}^2 p^2 + \frac{e^2\Phi^2}{4} + \frac{t_0^2}{2} - \sqrt{v_{\rm F}^2 p^2\left(e^2\Phi^2 + t_0^2\right) + \frac{t_0^4}{4}}} \tag{37}$$

depends on the absolute value of the vector $\mathbf{p}$. We propose the following ansatz for $\Delta^{\rm SC}_{\mathbf{k}}$:

$$\Delta^{\rm SC}_{\mathbf{K}_\xi + \mathbf{p}} = \begin{cases} \tilde{\Delta}^{\rm SC}_{\xi p} \cos\phi_{\mathbf{p}}, & |\mathbf{p}| < K_0, \\ 0 \quad \text{otherwise}, \end{cases} \tag{38}$$

where $\tilde{\Delta}^{\rm SC}_{\xi p}$ depends only on the absolute value of vector $\mathbf{p}$. We can show that near the Dirac points the following relation is true:

$$\Gamma^{\rm SC}_{\mathbf{K}_\xi + \mathbf{p}\mathbf{K}_\xi + \mathbf{p}'} = \tilde{\Gamma}^{\rm SC}(p,\ p',\ \phi_{\mathbf{p}} - \phi_{\mathbf{p}'}). \tag{39}$$

In this formula, the function $\tilde{\Gamma}^{\rm SC}(p,\ p',\ \phi_{\mathbf{p}} - \phi_{\mathbf{p}'})$ depends on the absolute values of the vectors $\mathbf{p}$ and $\mathbf{p}'$, and the polar angle $\phi_{\mathbf{p}} - \phi_{\mathbf{p}'}$ between them. Then, it is easy to derive

$$\int_0^{2\pi} \frac{d\phi'}{2\pi} \tilde{\Gamma}^{\rm SC}(p,\ p',\ \phi_{\mathbf{p}} - \phi')\cos\phi' = -\cos\phi_{\mathbf{p}} W(p,\ p'), \tag{40}$$

where the kernel $W$ is

$$W(p,\ p') = -\int_0^{2\pi} \frac{d\phi}{2\pi} \tilde{\Gamma}^{\rm SC}(p,\ p',\ \phi)\cos\phi. \tag{41}$$

The value $W(p,\ p')$ depends on the interactions $V^{ij}_{\mathbf{p}-\mathbf{p}'}$, which in turn depend on $q = |\mathbf{p} - \mathbf{p}'|$. The most important point for us here is that, when $q$ increases from 0 to $\sim 2k_{\rm F}^{(2)}$, the functions $V^{ij}_{\mathbf{q}}$ demonstrate a growing trend (see Fig. 5). As a result, the integral $\int d\phi \tilde{\Gamma}\cos\phi$ in Eq. (41) is negative at sufficiently small $p$ and $p'$, making $W(p,\ p')$ positive at small $p,\ p'$. Taking into account Eqs. (38), (39), (40), and (41),

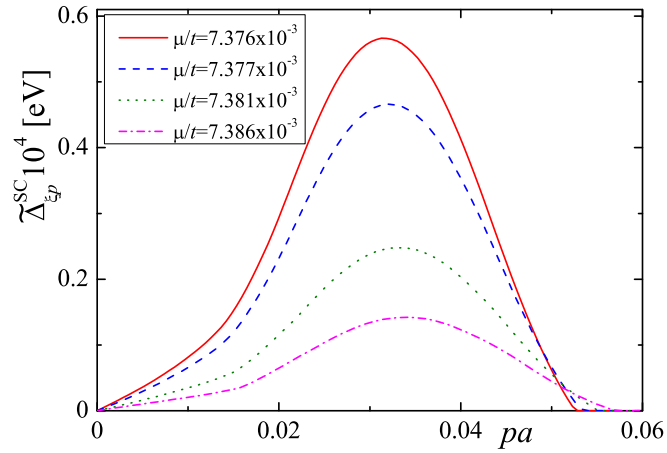


FIG. 6. The dependencies of the superconducting order parameter $\tilde{\Delta}^{\rm SC}_{\xi p}$ on $p$ calculated at $e\Phi = 0.1t_0 = 40$ meV and at four different values of the chemical potential (see the legend in the figure). For all curves, we take $\epsilon = 1$.

and neglecting the intervalley coupling, we can rewrite the self-consistency equation (35) in the form

$$\tilde{\Delta}^{\rm SC}_{\xi p} = \frac{\pi}{v_{\rm BZ}} \int_0^{K_0} p' dp' \frac{W(p,\ p')\tilde{\Delta}^{\rm SC}_{\xi p'}}{\sqrt{(\tilde{\varepsilon}_{p'} - \mu)^2 + \left(\tilde{\Delta}^{\rm SC}_{\xi p'}\right)^2}}. \tag{42}$$

We solve this integral equation numerically using the successive iterations technique. The typical curves $\tilde{\Delta}^{\rm SC}_{\xi p}$ versus $p$, calculated for $e\Phi = 0.1t_0 = 40$ meV, $\epsilon = 1$, and several values of $\mu$, are plotted in Fig. 6. In this figure, we observe that as $p$ grows, the function $\tilde{\Delta}^{\rm SC}_{\xi p}$ first increases from zero, and then, passing the maximum, it goes back to zero when $p \approx 4k_{\rm F}^{(2)}$. The order parameter $\tilde{\Delta}^{\rm SC}_{\xi p}$ vanishes at $p = 0$ because the integral over $\phi$ in Eq. (41) is zero when $p = 0$. At momenta $p \gtrsim 4k_{\rm F}^{(2)}$, we have $\tilde{\Delta}^{\rm SC}_{\xi p} = 0$ because the function $W(p,\ p')$ is negative at sufficiently large $p$ and $p'$.

Figure 7 shows the dependence of $\Delta^{\rm SC}_0 \equiv \max(\tilde{\Delta}^{\rm SC}_{\xi p})$ on the chemical potential. The value of $\Delta^{\rm SC}_0$ decreases with the increase of the chemical potential. We attribute such behavior to the fact that the density of states at the Fermi level decreases with $\mu$. Experimental data [16] also suggest that the large density of states is crucial for the superconductivity. The data in Fig. 7 indicate that, similar to the SDW case, the superconductivity weakens when $\epsilon$ increases.

The numerical results shown in Fig. 7 demonstrate that $\Delta^{\rm SC}_0$ can be as large as several hundred mK, which exceeds by an order of magnitude the superconducting transition temperature $T_c = 26$ mK measured experimentally [16]. To reconcile the theory with the experiment, let us estimate $T_c$ for our model. The finite-temperature generalization of the self-consistency equation (42) was derived using a standard technique, and it differs from the equation for $T = 0$ only by multiplication of the function under the integral by $\tanh[\sqrt{(\varepsilon_{p'} - \mu)^2 + \Delta^2_{\xi p'}}/(2T)]$. We solve numerically the self-consistency equation for $\tilde{\Delta}^{\rm SC}_{\xi p}$ at finite temperature $T$ for several values of $\mu$, and we observe a significant disparity between the order parameter and the transition temperature. For example, at $\mu/t = 7.374 \times 10^{-3}$, we could not find a

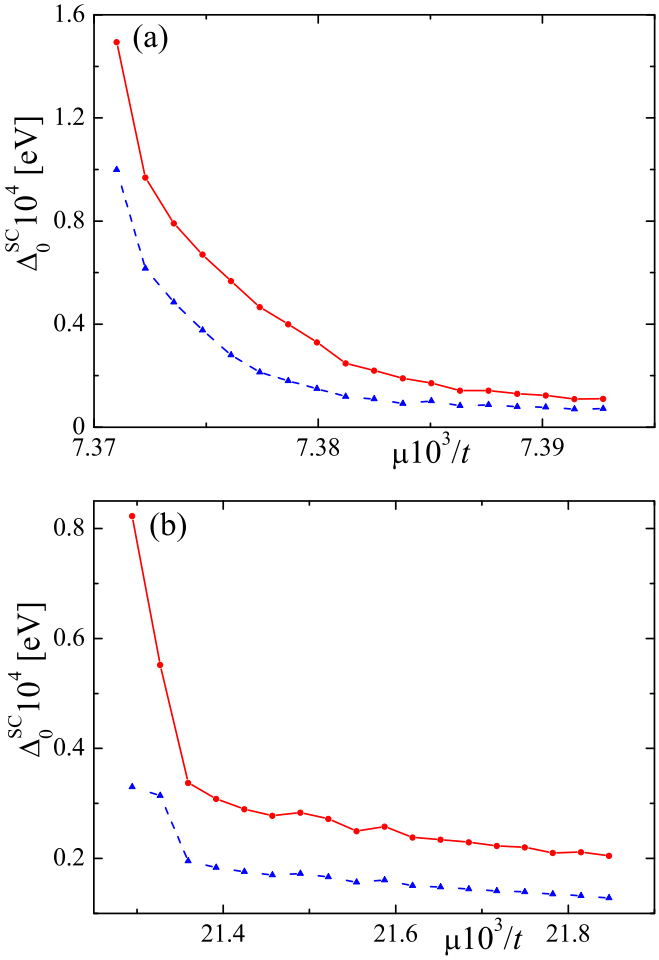


FIG. 7. The dependence of $\Delta_0^{SC} \equiv \max(\tilde{\Delta}_{\xi p}^{SC})$ on the chemical potential $\mu$ calculated for various values of the bias voltage $e\Phi$ and dielectric constant $\epsilon$. Panel (a) presents the data for $e\Phi = 0.1t_0 =$ 40 meV, while the curves in panel (b) are plotted for $e\Phi = 0.3t_0 =$ 120 meV. In both panels, the (red) solid curves with filled circles correspond to $\epsilon = 1$. The (blue) dashed curves with filled triangles correspond to $\epsilon = 5$.

nontrivial solution $\tilde{\Delta}_{\xi p}^{SC} \neq 0$ when $T > 23$ mK, which is $\approx 0.11\Delta_0^{SC} \ll \Delta_0^{SC}$. Therefore, for this value of $\mu$ the transition temperature is about 23 mK, which agrees well with the experiment. We associate that "strange" feature of our model, $T_c \ll \Delta_0^{SC}$, with the fact that the considered Fermi sea in the AB-BLG is very shallow: the Fermi energy defined as $\varepsilon_F = \mu - \mu_{\min}$ is comparable to, or even smaller than, $\Delta_0^{SC}$.

All the results above can be summarized in the phase diagram of the model in the $x$-$e\Phi$ plane. Let us consider first the SDW phase. For a given bias voltage $e\Phi$ the critical chemical potential $\mu_c^{SDW}$, above which the SDW state is suppressed, can be found from the equation [compare it with Eq. (25)]

$$\int_{|\mathbf{p}|<K_0} \frac{d^2\mathbf{p}}{v_{BZ}} \frac{\tilde{\Gamma}_{0\mathbf{p}}^{(1)} + \tilde{\Gamma}_{0\mathbf{p}}^{(2)}}{2\tilde{\varepsilon}_{\mathbf{p}}^{(3)}} \Theta\left(\tilde{\varepsilon}_{\mathbf{p}}^{(3)} - \mu\right) = 1. \tag{43}$$

Solving this equation and using Eq. (28), we obtain the curve $x_c^{SDW} = x_c^{SDW}(e\Phi)$ separating the SDW phase from the superconducting (SC) and paramagnetic (PM) phases. In

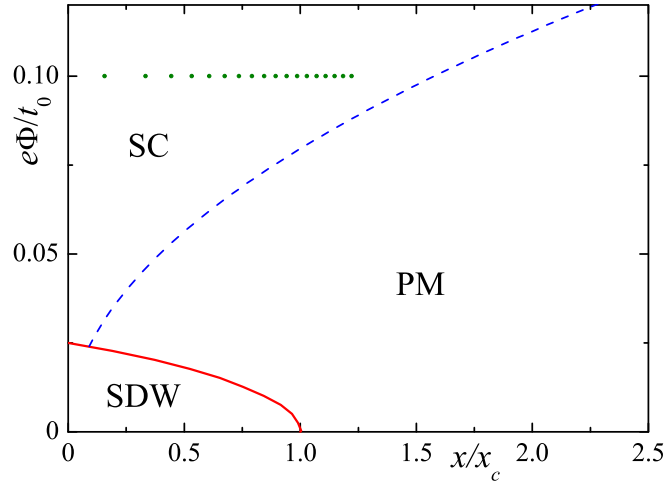


FIG. 8. Schematic phase diagram of the system in the $x$-$e\Phi$ plane. The red solid curve separates the SDW state from the SC and PM states. The blue dashed curve is the curve of the crossover between the SC and PM states. The critical doping $x_c$ corresponding to the SDW to PM transition at $\Phi = 0$ is estimated as $x_c \approx 1.3 \times 10^{-5}$ (for $t = 2.7$ eV, $t_0 = 0.4$ eV, and $\epsilon = 1$). Green circles depict the points $(x, e\Phi)$ at which the superconducting order parameter was calculated numerically [see Fig. 7(a)].

connection with the SC state, we restrict ourselves by considering the chemical potentials $\mu < e\Phi/2$ when the system has two Fermi surface sheets near each Dirac point. The case of larger chemical potentials requires separate analysis. Note, however, that for $\mu > e\Phi/2$ the superconducting order parameter, even if nonzero, will be small [see Eq. (27) and the text below it]. Thus, one can consider the curve $x_c^{SC}(e\Phi) = x(e\Phi/2) \approx e^2\Phi^2/(2\pi\sqrt{3}t^2)$ as the curve of the crossover between SC and PM states. The resultant phase diagram is shown in Fig. 8.

## VII. DISCUSSION AND CONCLUSIONS

We argued above that the doped and biased Bernal stacked bilayer graphene can host a Coulomb-interaction-driven triplet superconducting state. In this section, we will discuss certain important details of the mechanism that remain untouched in the more formal presentation.

### A. Kohn-Luttinger roots of superconductivity

The superconducting state becomes stable due to the fact that the functions $V_{\mathbf{q}}^{ij}$ increase with $q$ at small transferred momenta. Such a behavior of $V_{\mathbf{q}}^{ij}$ is obtained with the help of the RPA.

As the RPA is an uncontrollable approximation, one may wonder if our superconducting phase is indeed a genuine article, and not an artifact of careless theoretical assumptions. To allay those concerns, the validity of the RPA is discussed below; see Sec. VII B. In addition, we argue that our mechanism of superconductivity is not rooted in the particulars of the RPA approach. Rather, one can trace its origins to the proposal [37] of Kohn and Luttinger (KL).

It is instructive to compare the two mechanisms. Unlike our RPA-based formalism, the classical KL calculations [37] rely

on the second-order perturbation theory in powers of the bare Coulomb interaction. Since the second-order correction represents screening, it reduces the electron-electron repulsion. Loosely speaking, it is a kind of attraction that counteracts the bare Coulomb repulsion. Further, this correction is singular due to the Kohn anomaly in the polarization operator. KL's paper demonstrated that, for sufficiently large Cooper pair orbital momentum, the polarization operator, being singular, overcomes the nonsingular bare Coulomb interaction. In such an orbital channel, effective attraction emerges, leading to the superconducting instability.

The second-order correction, as a separate theoretical object, does not occur in our formalism. However, similar to the KL idea, the role of the polarization operator is quite essential for our mechanism as well. We see that the strong screening at low $q$ dominates in the effective interaction, as attested by the curves in Fig. 5. (This is particularly true for $V^{11}$ and $V^{12}$.) The polarization operator, controlling the renormalized interaction at small $q$, causes the overall growth of the effective interactions for growing $q$ in the interval $0.025 < qa < 0.1$. The latter growth of $V^{ij}_{\mathbf{q}}$ is the cornerstone of the mechanism suggested in Sec. VI.

### B. RPA validity

Let us briefly discuss to which extent the static RPA interaction can be considered as a reliable approach for our purposes. This problem contains two subproblems: (i) Is the RPA by itself reliable in our situation? (ii) Can the static version of the RPA effective interaction be used to study the SDW and superconductivity?

In connection to (i), let us consider the following. It is generally accepted that the RPA works well for phenomena involving distances greater than a characteristic screening (Debye) length $l_D$ [38–40]. From the data shown in Fig. 5, we can conclude that $l_D$ is of the order of $10\,a$, while the superconducting and SDW orders are determined mostly by the structure of the screened Coulomb interaction on scales larger than $l_D$. From our numerical results, it follows that the superconducting coherence length $\xi^{\mathrm{SC}} \sim \hbar v_{\mathrm{F}}^{(2)}/\Delta^{\mathrm{SC}}$ is about $100\,a$ in the parameter range of interest, which is larger than $l_D$. Moreover, it is commonly believed that using the RPA approach is especially reasonable for graphene-based systems since each bubble diagram enters the RPA expansion with a degeneracy factor $N_d = 4$ (this is due to the spin and valley degeneracies) [32].

(ii) The use of static effective interaction, as expressed in Eqs. (17) and (30), is valid as long as the full dynamic polarization operator $\Pi^{ij}_{\mathbf{q}}(\omega)$ does not vary significantly over the frequency scale set by the order parameter. For the SDW phase, the order parameter is several meV. Does $\Pi^{ij}_{\mathbf{q}}(\omega)$ for the undoped AB-BLG vary strongly over this scale? To answer this question, we want to make a simple observation. The only parameters entering $\Pi^{ij}_{\mathbf{q}}(\omega)$ are $t$ and $t_0$, both of which are much larger than $\Delta^{\mathrm{SDW}}$. This indicates clearly that, for $\omega$ limited to the interval whose width is of the order of $\Delta^{\mathrm{SDW}}$, the dynamical polarization operator may be safely approximated by its static version.

The situation with the superconducting phase requires more diligence: since the superconductivity is observed under the doping, in addition to the tunneling amplitudes, the Fermi energy enters $\Pi^{ij}_{\mathbf{q}}(\omega)$. Since $\varepsilon_{\mathrm{F}}$ is the smallest of the three energy parameters in $\Pi^{ij}_{\mathbf{q}}(\omega)$, we conclude that, when the superconducting energy scale does not exceed $\varepsilon_{\mathrm{F}}$, the static approximation works well.

### C. Magnetic field effect

In experiment [16], a superconducting state was observed only at finite in-plane magnetic field. This finding supports our assumption about the triplet structure of the superconducting order parameter. Indeed, it is known that the $p$-wave superconducting state, unlike its singlet counterpart, possesses a finite paramagnetic (Zeeman) susceptibility [41]. Consequently, the $p$-wave superconductivity is much more robust against applied magnetic field. We can speculate that, in the experiment, at finite applied field, the superconducting state replaces a nonsuperconducting phase that has lower zero-field energy but weaker Zeeman susceptibility. In such a scenario, application of the field can invert the relative stability of the two phases, leading to the realization of the superconductivity, which is metastable at zero field.

The nature of the phase supplanted by the superconductivity is an interesting question worth further research. For example, this phase can be one of several fractional metallic states (doped SDW with a spin- and valley-polarized Fermi surface), considered theoretically for graphene bilayer systems in Refs. [12,42]. Experimental results in Ref. [16] support such a hypothesis.

### D. Other types of superconducting order parameter

The superconducting order parameter discussed above is not the only possibility, as other types of superconductivity might be stabilized in our AB-BLG model. To illustrate this point, consider the following reasoning. The anomalous expectation $\eta^{\mathrm{SC}}_{\mathbf{k}} = \langle \gamma_{-\mathbf{k}3\sigma}\gamma_{\mathbf{k}3\sigma}\rangle$ suggested above couples electrons in different valleys, and the total momentum of the Cooper pair is zero. One can consider another choice, when both electrons constituting a pair belong to the same valley. The corresponding expectation value is $\tilde{\eta}^{\mathrm{SC}}_{\mathbf{p}\xi} = \langle \gamma_{\mathbf{K}_\xi-\mathbf{p}3\sigma}\gamma_{\mathbf{K}_\xi+\mathbf{p}3\sigma}\rangle$. The total momentum of such a pair is $2\mathbf{K}_\xi$. Consequently, the superconducting order parameter oscillates in real space, making this state a type of pair-density wave [43].

Since we limit ourselves to small doping, only one band crosses the Fermi level. The situation becomes richer at stronger doping, when two bands are partially filled. When this happens, an interband order parameter may be defined. It also oscillates in real space. However, the absence of van Hove singularities at higher $\mu$ implies that the corresponding condensation energy is low.

In general, the valley degeneracy is a peculiar feature of graphene-based materials, which introduces additional complications in the task of superconducting phase classification. Recent work [44] on the classification of nonsuperconducting phases in graphene bilayer demonstrated the challenges that one faces when the discrete index space grows twofold (from twofold spin degeneracy of BCS-like models to fourfold spin-valley degeneracy of graphene-based metals). In Ref. [44] we

offer an SU(4)-based approach to the nonsuperconducting-order classification that could possibly be extended to the superconducting phases as well.

### E. Trigonal warping

The single-particle Hamiltonian of our model is constructed under the assumption that the interlayer hopping occurs only between nearest-neighbor interlayer sites located in positions $1A$ and $2B$, and more distant interlayer hoppings are neglected. When this simplification is lifted, the low-energy electronic spectrum experiences certain modifications. For example, in the case $e\Phi = 0$, if we include the hopping amplitude $t_3$ between nearest-neighbor sites in positions $1B$ and $2A$ (see, e.g., Ref. [4]), two parabolic bands touching each other at the Dirac points are converted to four Dirac cones located near the Dirac points. Such a low-energy structure is called trigonal warping. Incorporation of the trigonal warping in our model alters the results in some aspects. First, it can change the estimate of the value of the SDW order parameter. Strictly speaking, Eq. (24) has a solution for arbitrarily small interaction, since the integral on the right-hand side of this equation diverges logarithmically when $\Delta_\xi^{\mathrm{SDW}} \to 0$. If the trigonal warping is taken into account, the nontrivial solution to Eq. (24) appears only at finite interaction strength, since the density of states vanishes at zero energy. However, the analysis reveals that the interaction is rather strong, while the trigonal warping modifies the electron spectrum only at energies about 1 meV (see, e.g., Ref. [4]), thus we expect that the estimate for the SDW order parameter does not change substantially when the trigonal warping is accounted for.

The trigonal warping, of course, transforms the low-energy spectrum of the AB-BLG, which affects the superconducting state. We believe, however, that the trigonal warping does not change our results qualitatively. Studies of the superconducting state via the renormalized Coulomb interaction, which take into account the trigonal warping, have been reported in Refs. [21,22]. The characteristic critical temperatures found there are consistent with our results.

### F. The role of the order parameter fluctuations

In two-dimensional systems, finite-temperature fluctuations of the Goldstone modes destroy any non-Ising long-range order. Specifically, in the SDW phase [45] the Goldstone mode is the spin-wave excitations described by the O(3) nonlinear $\sigma$ model in $(2+1)$-dimensional space. As temperature grows, the O(3) field correlations smoothly decay. As a result, a continuous transition, expected within the mean-field framework, is replaced by a smooth crossover. It is expected that the characteristic crossover temperature $T_*^{\mathrm{SDW}}$ is of order of the mean-field transition temperature

$$T_*^{\mathrm{SDW}} \sim T_{\mathrm{MF}}^{\mathrm{SDW}} \sim \Delta^{\mathrm{SDW}}. \tag{44}$$

This relation indicates that, for $0 < T \ll \Delta^{\mathrm{SDW}}$, robust signatures of short-range SDW order must be detectable experimentally.

Now we discuss the superconducting state. Since the bilayer sample is very thin, the magnetic field screening by the superconducting currents may be neglected. In such a situation, the fluctuations of the complex phase of $\Delta^{\mathrm{SC}}$ can be described by the $XY$ nonlinear $\sigma$ model. At sufficiently large $T$, this model demonstrates the Berezinskii-Kosterlitz-Thouless transition whose critical temperature, similar to estimate (44), is of the order of the mean-field critical temperature $T_c$.

### G. The role of the substrate's dielectric constant

Our calculations show that both the SDW and the superconductivity are weakened when the dielectric constant of the substrate grows. This is a straightforward consequence of the fact that both ordered states rely on the long-range Coulomb interaction. At the same time, these phases have dissimilar sensitivities to the increase of $\epsilon$. Specifically, we have seen that the growth of the dielectric constant from $\epsilon = 1$ to 5 suppresses the SDW order parameter by more than an order of magnitude. In contrast, the characteristic values of the superconducting order parameter decrease roughly twofold at most. This suggests that a substrate with a larger dielectric constant shifts the balance between the SDW and the superconductivity in favor of the latter. Such a possibility can be tested experimentally. One must remember, however, that here we ignore short-range interactions, which are insensitive to screening but may affect the properties of the ordered states. If these contributions are indeed significant in AB-BLG, the expected effect of $\epsilon$ might be weak.

### H. Conclusions

In this paper, we suggested a mechanism of superconductivity in the AB-BLG. This mechanism is based on the renormalized Coulomb electron-electron repulsion, and is similar in certain aspects to the Kohn-Luttinger mechanism. The superconducting state competes against the spin-density-wave state, which is also stabilized by the Coulomb interaction. The superconductivity in the proposed model has a $p$-wave structure. Our estimate for the critical temperature, as well as order parameter sensitivity to the doping, is consistent with recent experiment. Likewise, an in-plane magnetic field as a stabilization factor of the superconducting phase fits the proposed theoretical framework.

### ACKNOWLEDGMENT

This work is supported by RSF Grant No. 22-22-00464 [46].

## APPENDIX A: CHARGE-CONJUGATION SYMMETRY OF BIASED UNDOPED AB-BLG

Here we prove that our model is invariant under a certain charge-conjugation transformation. This invariance explains why the polarization operator components $\Pi_{\mathbf{q}}^{11}$ and $\Pi_{\mathbf{q}}^{22}$ are equal to each other as long as AB-BLG remains undoped. To start the discussion, we rewrite the matrix $\mathcal{H}_{\mathbf{k}}$ from Eq. (1) as follows:

$$\mathcal{H}_{\mathbf{k}} = \frac{e\Phi}{2}\tau_z - t\mathbf{f}\cdot\boldsymbol{\nu} + \frac{t_0}{4}[(\nu_x + i\nu_y)(\tau_x + i\tau_y) + (\nu_x - i\nu_y)(\tau_x - i\tau_y)], \tag{A1}$$

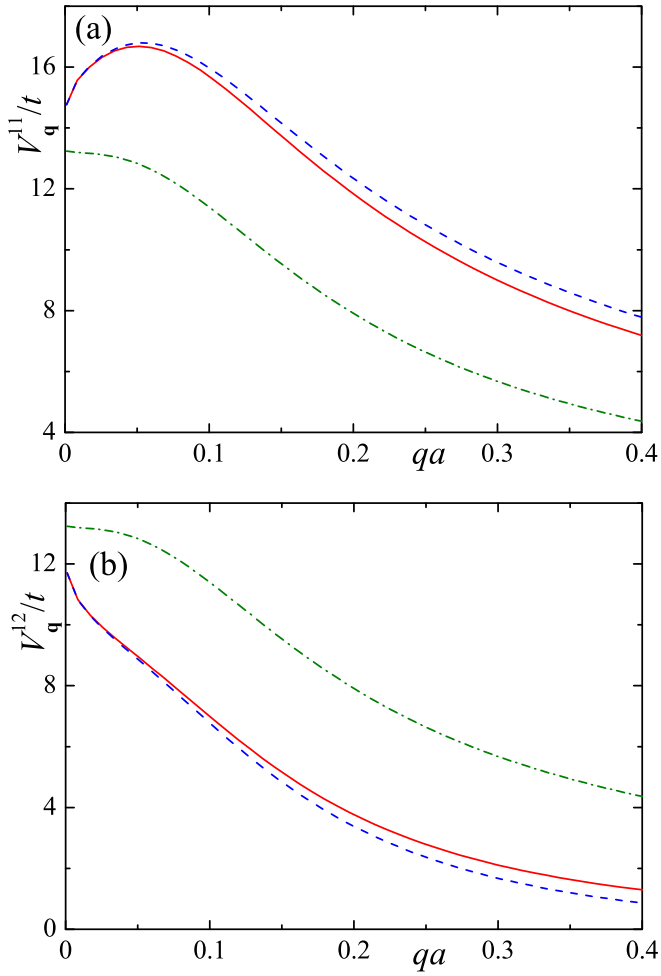


FIG. 9. The renormalized interaction components $V_{\mathbf{q}}^{ij}$ as functions of $q$, calculated using different approximations; $\mathbf{q} = q(1,\,0)$, $\mu = 0$, and $e\Phi = 0$. Panel (a) shows $V_{\mathbf{q}}^{11}$, while panel (b) shows $V_{\mathbf{q}}^{12}$. In both panels, the RPA interaction components, Eqs. (13) and (14), are plotted as a (red) solid curve, while approximate expressions (B1) and (B2) are represented by (blue) dashed curves. Dash-dotted (green) curves correspond to approximation (B3). We see that Eqs. (B1) and (B2) work quite well for small $q$, while formula (B3) is a very crude approximation for our choice of parameters.

where the Pauli matrices $\nu_i$ act in the sublattice space, while another set of Pauli matrices $\tau_i$ acts in the layer space, and $\mathbf{f}\cdot\boldsymbol{\nu} = \nu_x \mathrm{Re}\,(f_{\mathbf{k}}) - \nu_y \mathrm{Im}\,(f_{\mathbf{k}})$. For such a matrix, an equality

$$\nu_y\tau_x\mathcal{H}_{\mathbf{k}}^{*}\nu_y\tau_x = -\mathcal{H}_{\mathbf{k}} \tag{A2}$$

holds true. This relation is the signature of the charge-conjugation symmetry. To reveal the invariance of $H_0$ under the charge conjugation, we turn our attention to the second-quantization formalism. We write

$$H_0 = \sum_{\mathbf{k}\sigma}\sum_{\zeta\zeta'}[\mathcal{H}_{\mathbf{k}}]_{\zeta\zeta'}d^{\dagger}_{\mathbf{k}\zeta\sigma}d_{\mathbf{k}\zeta'\sigma}, \tag{A3}$$

where $[\mathcal{H}_{\mathbf{k}}]_{\zeta\zeta'}$ are matrix elements of $\mathcal{H}_{\mathbf{k}}$, and summation variables $\zeta$, $\zeta'$ are multi-indices containing layer and sublattice labels: $\zeta = (i,\alpha)$.

If we apply a charge-conjugation Bogoliubov transformation

$$d_{\mathbf{k}\zeta\sigma} \leftrightarrow d^{\dagger}_{\mathbf{k}\zeta\sigma}, \tag{A4}$$

the Hamiltonian $H_0$ transforms to

$$\begin{aligned} H_0^{\mathrm{C}} &= \sum_{\mathbf{k}\sigma}\sum_{\zeta\zeta'}[\mathcal{H}_{\mathbf{k}}]_{\zeta\zeta'}d_{\mathbf{k}\zeta\sigma}d^{\dagger}_{\mathbf{k}\zeta'\sigma} \\ &= \sum_{\mathbf{k}\sigma}\mathrm{Tr}\,\mathcal{H}_{\mathbf{k}} - \sum_{\mathbf{k}\sigma}\sum_{\zeta\zeta'}[\mathcal{H}_{\mathbf{k}}]_{\zeta\zeta'}d^{\dagger}_{\mathbf{k}\zeta'\sigma}d_{\mathbf{k}\zeta\sigma} \\ &= -\sum_{\mathbf{k}\sigma}\sum_{\zeta\zeta'}[\mathcal{H}^{*}_{\mathbf{k}}]_{\zeta\zeta'}d^{\dagger}_{\mathbf{k}\zeta\sigma}d_{\mathbf{k}\zeta'\sigma}, \end{aligned} \tag{A5}$$

where we used the fact that $\mathcal{H}_{\mathbf{k}}$ has zero trace for any $\mathbf{k}$, and $[\mathcal{H}_{\mathbf{k}}]_{\zeta\zeta'} = [\mathcal{H}^{*}_{\mathbf{k}}]_{\zeta'\zeta}$ due to hermiticity. Thus

$$H_0^{\mathrm{C}} = -\sum_{\mathbf{k}\sigma}\psi^{\dagger}_{\mathbf{k}\sigma}\mathcal{H}^{*}_{\mathbf{k}}\psi_{\mathbf{k}\sigma}. \tag{A6}$$

Defining the new operator vector $\psi^{\mathrm{C}}_{\mathbf{k}\sigma}$ by the relation

$$\psi_{\mathbf{k}\sigma} = \nu_y\tau_x\psi^{\mathrm{C}}_{\mathbf{k}\sigma}, \tag{A7}$$

we can confirm, using Eq. (A2), that $H_0^{\mathrm{C}}$ is unitarily equivalent to $H_0$.

At the same time, in the first-quantization formalism, Eq. (A2) implies that the transformation $\nu_y\tau_x\Psi^{(S)*}_{\mathbf{k}}$ converts the bispinor eigenvector $\Psi^{(S)}_{\mathbf{k}}$ corresponding to the energy $\varepsilon^{(S)}_{\mathbf{k}}$ into another bispinor eigenvector representing $-\varepsilon^{(S)}_{\mathbf{k}}$. Examining our definitions (6) one can check that $-\varepsilon^{(S)}_{\mathbf{k}} = \varepsilon^{(5-S)}_{\mathbf{k}}$. Thus, it is convenient to introduce the abbreviation $\bar{S} = 5 - S$. It allows us to write $\varepsilon^{(\bar{S})}_{\mathbf{k}} = -\varepsilon^{(S)}_{\mathbf{k}}$ and

$$\begin{aligned} \Psi^{(\bar{S})}_{\mathbf{k}1A} &= -i\Psi^{(S)*}_{\mathbf{k}2B}, \\ \Psi^{(\bar{S})}_{\mathbf{k}1B} &= i\Psi^{(S)*}_{\mathbf{k}2A}. \end{aligned} \tag{A8}$$

Substituting these formulas into expression (10) for $\Pi^{11}_{\mathbf{q}}$, and exploiting the relation

$$n_{\mathrm{F}}(\varepsilon) - n_{\mathrm{F}}(\varepsilon') = -[n_{\mathrm{F}}(-\varepsilon) - n_{\mathrm{F}}(-\varepsilon')], \tag{A9}$$

one can explicitly demonstrate that $\Pi^{11}_{\mathbf{q}} = \Pi^{22}_{\mathbf{q}}$.

Note that the Hamiltonian of the doped system does not possess this symmetry. Indeed, the charge conjugation inverts the sign of $\mu$, making the whole Hamiltonian noninvariant.

## APPENDIX B: APPROXIMATE EXPRESSION FOR THE SCREENED INTERACTION

Let us investigate here the accuracy of approximation (15). We assume that $\Pi^{11}_{\mathbf{q}} = \Pi^{22}_{\mathbf{q}}$ due to the charge-conjugation symmetry. In the limit $qd \ll 1$, we expand $\exp(-qd) \approx 1 - qd$ to derive

$$V^{11}_{\mathbf{q}} = V^{22}_{\mathbf{q}} = \frac{\frac{1}{2}\left(1-\mathcal{E}\Pi^{22}_{\mathbf{q}}\right)\mathcal{E}}{(qd)\left(1+\mathcal{E}\Pi^{12}_{\mathbf{q}}\right) - \mathcal{E}\left(1+\frac{1}{2}\mathcal{E}\Pi^{12}_{\mathbf{q}} - \frac{1}{2}\mathcal{E}\Pi^{11}_{\mathbf{q}}\right)\left(\Pi^{11}_{\mathbf{q}} + \Pi^{12}_{\mathbf{q}}\right)}, \tag{B1}$$

$$V_{\mathbf{q}}^{12} = V_{\mathbf{q}}^{21} = \frac{\frac{1}{2}\left(1 - qd + \mathcal{E}\Pi_{\mathbf{q}}^{12}\right)\mathcal{E}}{(qd)\left(1 + \mathcal{E}\Pi_{\mathbf{q}}^{12}\right) - \mathcal{E}\left(1 + \frac{1}{2}\mathcal{E}\Pi_{\mathbf{q}}^{12} - \frac{1}{2}\mathcal{E}\Pi_{\mathbf{q}}^{11}\right)\left(\Pi_{\mathbf{q}}^{11} + \Pi_{\mathbf{q}}^{12}\right)}, \tag{B2}$$

where we introduce the energy scale $\mathcal{E} = 2Ad$. For permittivity $\epsilon = 5$ one finds $\mathcal{E} = 23.2$ eV, or, equivalently, $\mathcal{E} = 8.6t$. This energy can be used to rewrite formula (15),

$$V_{\mathbf{q}}^{ij} = \frac{\frac{1}{2}\mathcal{E}}{(qd) - \mathcal{E}\left(\Pi_{\mathbf{q}}^{11} + \Pi_{\mathbf{q}}^{12}\right)}. \tag{B3}$$

Comparing this relation and Eqs. (B1) and (B2), one concludes that Eq. (B3) is valid only when $\mathcal{E}\Pi_{\mathbf{q}}^{ij}$ is much smaller than unity at small $qd$. However, for our model parameters, the quantity $\mathcal{E}\Pi_{\mathbf{q}}^{ij}$ is of order unity, making Eqs. (B3) and (15) a poor approximation. Figure 9 allows one to compare the accuracy of the two approximations.


[1] Y. Cao, V. Fatemi, A. Demir, S. Fang, S. L. Tomarken, J. Y. Luo, J. D. Sanchez-Yamagishi, K. Watanabe, T. Taniguchi, E. Kaxiras *et al.*, Correlated insulator behaviour at half-filling in magic-angle graphene superlattices, Nature (London) **556**, 80 (2018).

[2] Y. Cao, V. Fatemi, S. Fang, K. Watanabe, T. Taniguchi, E. Kaxiras, and P. Jarillo-Herrero, Unconventional superconductivity in magic-angle graphene superlattices, Nature (London) **556**, 43 (2018).

[3] X. Lu, P. Stepanov, W. Yang, M. Xie, M. A. Aamir, I. Das, C. Urgell, K. Watanabe, T. Taniguchi, G. Zhang *et al.*, Superconductors, orbital magnets and correlated states in magic-angle bilayer graphene, Nature (London) **574**, 653 (2019).

[4] A. Rozhkov, A. Sboychakov, A. Rakhmanov, and F. Nori, Electronic properties of graphene-based bilayer systems, Phys. Rep. **648**, 1 (2016).

[5] W. Bao, J. Velasco, F. Zhang, L. Jing, B. Standley, D. Smirnov, M. Bockrath, A. H. MacDonald, and C. N. Lau, Evidence for a spontaneous gapped state in ultraclean bilayer graphene, Proc. Natl. Acad. Sci. USA **109**, 10802 (2012).

[6] J. Velasco, L. Jing, W. Bao, Y. Lee, P. Kratz, V. Aji, M. Bockrath, C. N. Lau, C. Varma, R. Stillwell *et al.*, Transport spectroscopy of symmetry-broken insulating states in bilayer graphene, Nat. Nanotechnol. **7**, 156 (2012).

[7] A. Veligura, H. J. van Elferen, N. Tombros, J. C. Maan, U. Zeitler, and B. J. van Wees, Transport gap in suspended bilayer graphene at zero magnetic field, Phys. Rev. B **85**, 155412 (2012).

[8] F. Freitag, M. Weiss, R. Maurand, J. Trbovic, and C. Schönenberger, Spin symmetry of the bilayer graphene ground state, Phys. Rev. B **87**, 161402(R) (2013).

[9] J. Nilsson, A. H. Castro Neto, N. M. R. Peres, and F. Guinea, Electron-electron interactions and the phase diagram of a graphene bilayer, Phys. Rev. B **73**, 214418 (2006).

[10] T. C. Lang, Z. Y. Meng, M. M. Scherer, S. Uebelacker, F. F. Assaad, A. Muramatsu, C. Honerkamp, and S. Wessel, Antiferromagnetism in the hubbard model on the bernal-stacked honeycomb bilayer, Phys. Rev. Lett. **109**, 126402 (2012).

[11] Y. Wang, H. Wang, J.-H. Gao, and F.-C. Zhang, Layer antiferromagnetic state in bilayer graphene: A first-principles investigation, Phys. Rev. B **87**, 195413 (2013).

[12] A. L. Rakhmanov, A. V. Rozhkov, A. O. Sboychakov, and F. Nori, Half-metal and other fractional metal phases in doped *AB* bilayer graphene, Phys. Rev. B **107**, 155112 (2023).

[13] H. Min, G. Borghi, M. Polini, and A. H. MacDonald, Pseudospin magnetism in graphene, Phys. Rev. B **77**, 041407(R) (2008).

[14] O. Vafek and K. Yang, Many-body instability of Coulomb interacting bilayer graphene: Renormalization group approach, Phys. Rev. B **81**, 041401(R) (2010).

[15] S. C. de la Barrera, S. Aronson, Z. Zheng, K. Watanabe, T. Taniguchi, Q. Ma, P. Jarillo-Herrero, and R. Ashoori, Cascade of isospin phase transitions in Bernal-stacked bilayer graphene at zero magnetic field, Nat. Phys. **18**, 771 (2022).

[16] H. Zhou, L. Holleis, Y. Saito, L. Cohen, W. Huynh, C. L. Patterson, F. Yang, T. Taniguchi, K. Watanabe, and A. F. Young, Isospin magnetism and spin-polarized superconductivity in Bernal bilayer graphene, Science **375**, 774 (2022).

[17] A. M. Seiler, F. R. Geisenhof, F. Winterer, K. Watanabe, T. Taniguchi, T. Xu, F. Zhang, and R. T. Weitz, Quantum cascade of correlated phases in trigonally warped bilayer graphene, Nature (London) **608**, 298 (2022).

[18] Y.-Z. Chou, F. Wu, J. D. Sau, and S. Das Sarma, Acoustic-phonon-mediated superconductivity in Bernal bilayer graphene, Phys. Rev. B **105**, L100503 (2022).

[19] Y.-Z. Chou, F. Wu, J. D. Sau, and S. Das Sarma, Acoustic-phonon-mediated superconductivity in moiréless graphene multilayers, Phys. Rev. B **106**, 024507 (2022).

[20] A. L. Szabó and B. Roy, Competing orders and cascade of degeneracy lifting in doped Bernal bilayer graphene, Phys. Rev. B **105**, L201107 (2022).

[21] A. Jimeno-Pozo, H. Sainz-Cruz, T. Cea, P. A. Pantaleón, and F. Guinea, Superconductivity from electronic interactions and spin-orbit enhancement in bilayer and trilayer graphene, Phys. Rev. B **107**, L161106 (2023).

[22] G. Wagner, Y. H. Kwan, N. Bultinck, S. H. Simon, and S. A. Parameswaran, Superconductivity from repulsive interactions in Bernal-stacked bilayer graphene, arXiv:2302.00682.

[23] Z. Dong, A. V. Chubukov, and L. Levitov, Transformer spin-triplet superconductivity at the onset of isospin order in bilayer graphene, Phys. Rev. B **107**, 174512 (2023).

[24] T. Cea, Superconductivity induced by the intervalley Coulomb scattering in a few layers of graphene, Phys. Rev. B **107**, L041111 (2023).

[25] X.-F. Wang and T. Chakraborty, Coulomb screening and collective excitations in a graphene bilayer, Phys. Rev. B **75**, 041404(R) (2007).

[26] X.-F. Wang and T. Chakraborty, Coulomb screening and collective excitations in biased bilayer graphene, Phys. Rev. B **81**, 081402(R) (2010).
[27] M. Lv and S. Wan, Screening-induced transport at finite temperature in bilayer graphene, Phys. Rev. B **81**, 195409 (2010).
[28] E. H. Hwang and S. Das Sarma, Screening, kohn anomaly, friedel oscillation, and RKKY interaction in bilayer graphene, Phys. Rev. Lett. **101**, 156802 (2008).
[29] R. Sensarma, E. H. Hwang, and S. Das Sarma, Dynamic screening and low-energy collective modes in bilayer graphene, Phys. Rev. B **82**, 195428 (2010).
[30] O. V. Gamayun, Dynamical screening in bilayer graphene, Phys. Rev. B **84**, 085112 (2011).
[31] C. Triola and E. Rossi, Screening and collective modes in gapped bilayer graphene, Phys. Rev. B **86**, 161408(R) (2012).
[32] V. N. Kotov, B. Uchoa, V. M. Pereira, F. Guinea, and A. H. Castro Neto, Electron-electron interactions in graphene: Current status and perspectives, Rev. Mod. Phys. **84**, 1067 (2012).
[33] A. Kamenev and Y. Oreg, Coulomb drag in normal metals and superconductors: Diagrammatic approach, Phys. Rev. B **52**, 7516 (1995).
[34] K. Flensberg, B. Y.-K. Hu, A.-P. Jauho, and J. M. Kinaret, Linear-response theory of Coulomb drag in coupled electron systems, Phys. Rev. B **52**, 14761 (1995).
[35] A. S. Mayorov, D. C. Elias, M. Mucha-Kruczynski, R. V. Gorbachev, T. Tudorovskiy, A. Zhukov, S. V. Morozov, M. I. Katsnelson, V. I. Fal'ko, A. K. Geim *et al.*, Interaction-driven spectrum reconstruction in bilayer graphene, Science **333**, 860 (2011).
[36] F. Freitag, M. Weiss, R. Maurand, J. Trbovic, and C. Schönenberger, Homogeneity of bilayer graphene, Solid State Commun. **152**, 2053 (2012).
[37] W. Kohn and J. M. Luttinger, New mechanism for superconductivity, Phys. Rev. Lett. **15**, 524 (1965).
[38] D. Pines and D. Bohm, A collective description of electron interactions: II. Collective vs individual particle aspects of the interactions, Phys. Rev. **85**, 338 (1952).
[39] G. D. Mahan, *Many-Particle Physics* (Springer Science & Business Media, 2000).
[40] H. Bruus and K. Flensberg, *Many-Body Quantum Theory in Condensed Matter Physics: An Introduction* (Oxford University Press, Oxford, 2004).
[41] V. Mineev and K. Samokhin, *Introduction to Unconventional Superconductivity* (Taylor & Francis, Amsterdam, 1999).
[42] A. O. Sboychakov, A. L. Rakhmanov, A. V. Rozhkov, and F. Nori, Bilayer graphene can become a fractional metal, Phys. Rev. B **103**, L081106 (2021).
[43] H.-D. Chen, O. Vafek, A. Yazdani, and S.-C. Zhang, Pair density wave in the pseudogap state of high temperature superconductors, Phys. Rev. Lett. **93**, 187002 (2004).
[44] A. V. Rozhkov, A. O. Sboychakov, and A. L. Rakhmanov, Ordering in SU(4)-symmetric model of AA bilayer graphene, arXiv:2306.05796.
[45] A. O. Sboychakov, A. V. Rozhkov, A. L. Rakhmanov, and F. Nori, Antiferromagnetic states and phase separation in doped *AA*-stacked graphene bilayers, Phys. Rev. B **88**, 045409 (2013).
[46] https://rscf.ru/en/project/22-22-00464/.